

Novel Insights into Sb-Cu Catalysts for Electrochemical Reduction of CO<sub>2</sub>

Juqin Zeng<sup>a,\*</sup>, Michele Re Fiorentin<sup>a</sup>, Marco Fontana<sup>a</sup>, Micaela Castellino<sup>b,\*\*</sup>,  
 Francesca Risplendi<sup>b</sup>, Adriano Sacco<sup>a</sup>, Giancarlo Cicero<sup>b,\*\*</sup>, M.Amin Farkhondeh<sup>a</sup>,  
 Filippo Drago<sup>c</sup>, Candido F. Pirri<sup>a,b</sup>

<sup>a</sup> Center for Sustainable Future Technologies @POLITO, Istituto Italiano di Tecnologia, Via Livorno 60, 10144 Turin, Italy

<sup>b</sup> Department of Applied Science and Technology, Politecnico di Torino, C.so Duca degli Abruzzi 24, 10129 Turin, Italy

<sup>c</sup> NanoChemistry, Istituto Italiano di Tecnologia, via Morego 30, 16163 Genoa, Italy

## ARTICLE INFO

## Keywords:

Carbon dioxide

Electrocatalysis

Cuprous oxide

Antimony

Ab initio simulation

## ABSTRACT

Catalysts play a vital role in electrochemical reduction of CO<sub>2</sub> to valuable products. Only based on effective catalysts, CO<sub>2</sub> electrolysis process can be advanced toward industrial application. In this work, we present a Sb-Cu<sub>2</sub>O material synthesized via one-pot microwave-assisted solvothermal route. The Sb-Cu<sub>2</sub>O derived bimetallic catalyst achieves a highest CO selectivity of 96% and good CO partial current densities of 37.3 and 74.0 mA cm<sup>-2</sup> at -0.8 and -1.2 V vs. reversible hydrogen electrode (RHE), respectively. The Sb-Cu catalyst also displays good stability at current densities ranging from 5.6 to 100 mA cm<sup>-2</sup>. Additionally, for the first time, a complete theoretical study reveals the critical roles of Sb in selective CO<sub>2</sub> conversion to CO on this bimetallic material, including stabilizing stepped Cu surfaces selective for the reaction, lowering energy barriers for the formation of key intermediate and favouring CO desorption.

## 1. Introduction

Excessive CO<sub>2</sub> emitted from burning fossil fuels is considered one of the main climate change causes. Strategies such as CO<sub>2</sub> capture and storage have been applied, aiming at decelerating and even at discontinuing the accumulation of CO<sub>2</sub> in the atmosphere. Further transformation of the captured CO<sub>2</sub> into fuels and chemicals is of crucial importance for a sustainable carbon cycle and the long-term energy storage. Among many technologies, electrochemical conversion is considered particularly attractive since it can use electricity generated from renewable sources as energy input [1–5]. This technology, although being very promising, confronts many challenges due to the high energy barriers, slow kinetics and complex pathways of the CO<sub>2</sub> reduction reaction (CO<sub>2</sub>RR). Therefore, rationally designed electrocatalysts are essential to boost the reaction and to tune the selectivity for a specific product. In the last decades, copper (Cu) has received the greatest attention as electrocatalytic material for the CO<sub>2</sub>RR, due to its unique properties from the early experimental studies by Hori et al. [6, 7] as well as the computational investigations by Nørskov et al. [8,9] and Bagger et al. [10]. Except bulk Cu and nanostructured Cu [11–15], Cu-based bimetallic systems have been widely explored and they

demonstrated the most encouraging performance [16–19]. Among many secondary metals, post-transition metals such as tin (Sn), indium (In) and bismuth (Bi) are intensively studied since they alone are demonstrated to be active for the CO<sub>2</sub>RR and coupling them with Cu can catalyze the CO<sub>2</sub>RR to carbon monoxide (CO) and formate (HCOO<sup>-</sup>) selectively [20–25]. Even though antimony (Sb) is adjacent to these metals in the periodic table, it has attracted negligible attention in the community of the electrochemical CO<sub>2</sub>RR, probably due to the poor performance of the electrodeposited Sb reported earlier by Rosenthal et al. [26]. Until 2017, Zhang et al. [27] reported two-dimensional “few-layer” Sb nanosheets (SbNSs) that deliver a maximum faradaic efficiency (FE) of 84% and a maximum geometric current density of 3.1 mA cm<sup>-2</sup> for formate production at potentials from -0.7 V to -1.4 V vs. the reversible hydrogen electrode (RHE) in a CO<sub>2</sub>-saturated 0.5 M NaHCO<sub>3</sub> solution. In 2019, Sun et al. [28] synthesized Sb single atoms supported on N-doped porous carbon that reached an FE of about 82.0% and a highest current density of 2.4 mA cm<sup>-2</sup> for CO formation at -0.9 V vs. RHE in a CO<sub>2</sub>-saturated 0.1 M KHCO<sub>3</sub> solution. It is only very recently that Cu-Sb bimetallic materials were proposed for the CO<sub>2</sub>RR, achieving good CO selectivity of 85–90% [29–32] and moderate C<sub>2</sub>H<sub>4</sub> selectivity of 49.7% [33]. Among these work, only Cai et al. [32]

\* Corresponding author.

\*\* Corresponding authors.

E-mail addresses: [juqin.zeng@iit.it](mailto:juqin.zeng@iit.it) (J. Zeng), [micaela.castellino@polito.it](mailto:micaela.castellino@polito.it) (M. Castellino), [giancarlo.cicero@polito.it](mailto:giancarlo.cicero@polito.it) (G. Cicero).

<https://doi.org/10.1016/j.apcatb.2022.121089>

Received 18 August 2021; Received in revised form 5 January 2022; Accepted 7 January 2022

Available online 12 January 2022

0926-3373/© 2022 Elsevier B.V. All rights reserved.

performed a theoretical study through Density Functional Theory (DFT) calculations by designing a thermodynamic structure model of the Sb/Cu surface that considers the lattice mismatch between Cu and Sb at a high Sb coverage. The DFT study qualitatively consists with the in situ ATR-SEIRAS experimental observations, suggesting that the weak bonding of  $^*CO$  on Cu-Sb favors CO desorption and ultimately promotes CO formation. Despite the significance of this work, the good selectivity toward CO production against the competing hydrogen evolution reaction (HER) and HCOOH formation, and the possible reaction pathways are not explained. So far, a thorough understanding of the electrochemical performance of Cu-Sb materials still calls for additional insights into the role of Sb and into the mechanisms of the competing CO<sub>2</sub>RR and HER.

The present study couples Sb and Cu for the CO<sub>2</sub>RR and, for the first time, explores the origin of the high CO selectivity and the reaction mechanism on the bimetallic catalyst through a complete theoretical study. Several Sb incorporated Cu<sub>2</sub>O powder-like materials were synthesized via a one-pot microwave-assisted solvothermal route. The optimal Sb-Cu catalyst derived from Sb-Cu<sub>2</sub>O is characterized by an outstanding CO selectivity (FE<sub>CO</sub> 90–95%) in a wide potential window from  $-0.7$  V to  $-1.2$  V vs. RHE in 0.1 M KHCO<sub>3</sub> aqueous electrolyte. With increasing KHCO<sub>3</sub> concentration, the good CO selectivity is maintained and a highest CO partial current density of  $74.2 \text{ mA cm}^{-2}$  is observed. By means of ab initio simulations based on DFT and the Cluster Expansion (CE) method, we correlated the striking selectivity toward CO production to the change in Cu surface stability induced by Sb atoms. Under CO<sub>2</sub>RR conditions, Cu<sub>2</sub>O is reduced to metal Cu and Sb tends to segregate to the surface. Optimal surface concentrations of Sb appear to favor the exposure of stepped and reactive surface, on which CO<sub>2</sub> is selectively reduced to CO thanks to the lower kinetic barriers. In addition, the reaction mechanism was also illustrated by the theoretical study combining with electrokinetic experimental data.

## 2. Material and methods

### 2.1. Chemicals

Antimony(III) acetate (Sb(OAc)<sub>3</sub>, 99.99%), Copper(II) acetate hydrate (Cu(OAc)<sub>2</sub>·xH<sub>2</sub>O, 98.0%), potassium bicarbonate (KHCO<sub>3</sub>, 99.7%), ethylene glycol (EG, 99.8%), Nafion® 117 solution (5 wt%) and isopropanol were purchased from Sigma-Aldrich. Unless otherwise specified, all the materials were used as received in this work.

### 2.2. Synthesis of Sb-Cu<sub>2</sub>O materials

The pre-catalysts Sb-Cu<sub>2</sub>O were fabricated through a microwave-assisted solvothermal route. Four Sb-Cu<sub>2</sub>O materials were synthesized and named Sb<sub>x</sub>Cu<sub>2</sub>O ( $x = 0.11, 0.22, 0.33$  and  $0.55$ ), where  $x$  was the nominal atomic ratio of Sb(OAc)<sub>3</sub>/Cu(OAc)<sub>2</sub> in the precursor solution. Two samples with only Sb or Cu precursor were also prepared and named Sb<sub>2</sub>O<sub>3</sub> and Cu<sub>2</sub>O, respectively. The details of the synthesis are shown in the *Synthesis* section and Table S1 of the [supporting information](#).

### 2.3. Physical and chemical characterizations

The morphology was studied by Field Emission Scanning Electron Microscopy (FESEM, ZEISS Supra 40). X-ray diffraction (XRD) was performed in Bragg-Brentano symmetric geometry by using a PANalytical X'Pert Pro instrument (Cu-K $\alpha$  radiation, 40 kV and 30 mA) equipped with an X'Celerator detector. MAUD software [34] was used for full XRD pattern fitting based on the Rietveld method (XRD characterization section of [supporting information](#)). Transmission Electron Microscopy (TEM) was carried out on a FEI Tecnai G2 F20 S-Twin instrument, operated at 200 kV acceleration voltage. The microscope is equipped with a EDAX detector (30 mm<sup>2</sup> active area, Si(Li) technology)

for Energy-Dispersive X-ray spectroscopy (EDX). Regarding TEM sample preparation, the dry powders were dispersed in high-purity ethanol, sonicated for 30 min and subsequently drop-casted on Au holey carbon grids. The sonication time was chosen in accordance with the electrode preparation procedure. X-ray photoelectron spectroscopy (XPS) analysis has been performed by means of a PHI 5000 Versaprobe spectrometer, equipped with a monochromated Al K-alpha source (1486.6 eV). A double charge compensation system, comprised of an electron and Ar<sup>+</sup> ion gun, was used to neutralize surface charging. Survey and high resolution (HR) spectra were acquired using Pass Energy (PE) values of 187.85 and 23.50 eV, respectively. C1s peak at 284.5 eV was chosen as the reference shift. Tougaard background function was subtracted from HR spectra to remove background signal and pseudo-Voigt functions were used to deconvolute the HR curves. Casa XPS Version 2.3.18 dedicated software has been used to analyze the raw spectra.

### 2.4. Electrode preparation, electrochemical tests and product analyses

The pre-catalysts were coated onto a carbon paper, as detailed in the *Electrode preparation* section of [supporting information](#), in order to enable the electrochemical evaluation of the materials toward the CO<sub>2</sub>RR. Cyclic voltammetry (CV), linear sweep voltammetry (LSV) and electrochemical impedance spectroscopy (EIS) were performed in a three-electrode single-compartment cell at room temperature with a CHI760D electrochemical workstation, as described in the *Electrochemical characterizations* section of [supporting information](#).

The CO<sub>2</sub>RR experiments in KHCO<sub>3</sub> electrolyte were conducted in a custom-made H-type cell ([Fig. S1a](#)) and those in KOH electrolyte were carried out in a custom-made flow cell ([Fig. S1b](#)). Chronoamperometric (CA) technique was applied for the CO<sub>2</sub>RR with a CHI760D electrochemical workstation. The *Electrochemical characterizations* section of [supporting information](#) shows the details of the cells and processes. The reported potentials were corrected by compensating 85% of the ohmic drop (iR-compensation). Electrode potentials after iR-compensation were rescaled to the RHE reference by applying Nernst equation,  $E_{\text{vs. RHE}} = E_{\text{vs. Ag/AgCl}} + E_{\text{Ag/AgCl}}(3 \text{ M Cl}^-) + 0.0591 \times \text{pH}$ .

Gas-phase products were analyzed on-line with a micro gas chromatograph ( $\mu$ GC, Fusion®, INFICON) and liquid products were analyzed by a High Performance Liquid Chromatograph (ThermoFischer Ultimate 3000), as detailed in the *Product analysis* section of [supporting information](#).

### 2.5. Mass transport model

The local concentrations of CO<sub>2</sub> and HCO<sub>3</sub><sup>-</sup> in proximity of the electrode ( $[CO_2]_{\text{local}}$  and  $[HCO_3^-]_{\text{local}}$ ) in different bulk  $[HCO_3^-]$  electrolytes were calculated employing the mass transport model described in details in our previous work [35]. The diffusion coefficients and the equilibrium concentrations of various chemical species as well as the electrolyte viscosity are dependent on the bulk  $[HCO_3^-]$  and different values were used for 0.1 M, 0.5 M, 1.0 M and 2.0 M KHCO<sub>3</sub> electrolyte [36]. Correction was not made for the effect of ionic strength on CO<sub>2</sub> solubility.

### 2.6. Computational methods

When working under potentials and pH values suitable for CO<sub>2</sub> electroreduction, Cu oxides are rapidly reduced to metallic Cu [37], whose most stable surface can then be assumed to be most largely involved in the CO<sub>2</sub>RR. However, the presence of Sb atoms dispersed in metallic Cu can significantly affect the surface stability and, in turn, the activity and selectivity of the catalyst. The prediction of the structure and stability of Sb modified Cu surfaces has been carried out by combining DFT and CE methods. CE simulations were performed by employing the ATAT software [38], while for the DFT calculations the QUANTUM ESPRESSO software package was used [39,40]. The coupled

CE-DFT approach makes it possible to accurately predict concentration-dependent phase diagrams and surface phase diagrams of a given alloy, following a step-by-step process based on alternating DFT total energy calculations and CE structural predictions [41]. Details on this procedure can be found in the [Supporting Information](#) and in the literature [42,43]. The analysis of electrochemical reactions on the catalyst was carried out within the computational hydrogen electrode framework [44], which allows obtaining reaction free energies as a function of the applied potential. A correction to the adsorbate free energies was added to account for solvation effects due to the aqueous environment [8]. Activation barriers for each reduction reaction step were obtained with nudged elastic band (NEB) calculations at the equilibrium potential of the relative step, and their values at different potentials were derived within the Butler-Volmer formalism [45–47]. Activation barriers for the HER were obtained from the literature [48].

### 3. Results and Discussion

#### 3.1. Synthesis and characterization of $Sb_xCu_2O$ pre-catalysts

[Fig. 1a](#) illustrates the synthesis of pre-catalysts via one-pot microwave-assisted solvothermal method. The obtained  $Cu_2O$  sample is composed of submicrometric cubic and micrometric polyhedral aggregates with irregular external surface populated by nanoplatelets ([Fig. 1b](#) and inset of [Fig. 1b](#)). The addition of Sb has remarkable effect on the

morphology of the materials. Uniform and large spheres (diameter in the range of 4–7  $\mu m$ ) are formed in all  $Sb-Cu_2O$  materials ([Fig. 1c-f](#)) and these spheres consist of loosely packed nanoparticles with diameter less than 15 nm (inset of [Fig. 1c-f](#)). The spheres become less compact with increasing the percentage of Sb salt in the precursor solution. The  $Sb_2O_3$  sample contains submicrometric rhombohedral particles with a wide size distribution from 500 nm to 800 nm ([Fig. 1g](#)). It is worth noting that similar particles of Sb species are also present in the  $Sb_{0.55}Cu_2O$  sample, while these particles are absent in the other  $Sb-Cu_2O$  materials.

XRD analysis has been employed to identify the crystalline phase compositions of the materials. The patterns of various materials and the fitting results obtained by Rietveld refinement are shown in [Fig. S2](#) and [Table S2](#). For the  $Cu_2O$  sample, all peaks are associated to the (110), (111), (200), (211), (220), (311) and (222) planes of  $Cu_2O$  with a cubic structure (JCPDS 00–005–0667). The  $Cu_2O$  phase has a bimodal crystallite size distribution centered at  $307 \pm 33$  nm and  $35 \pm 5$  nm. The  $Sb_2O_3$  sample exhibits peaks related to only the cubic  $Sb_2O_3$  (JCPDS 01–071–0365) structure, with a refined crystallite size of  $191 \pm 1$  nm. All  $Sb-Cu_2O$  materials show peaks corresponding to the cubic  $Cu_2O$  phase. No peaks related to crystalline Sb species are observed for the  $Sb_{0.11}Cu_2O$ ,  $Sb_{0.22}Cu_2O$  and  $Sb_{0.33}Cu_2O$  samples, while peaks associated to  $Sb_2O_3$  crystallite phase are present in the XRD pattern of the  $Sb_{0.55}Cu_2O$  sample. The  $Cu_2O$  crystallites in the  $Sb_{0.11}Cu_2O$  sample display a bimodal size distribution centered at  $86 \pm 4$  nm and  $9 \pm 1$  nm and the crystallite size values for the  $Sb_{0.22}Cu_2O$ ,  $Sb_{0.33}Cu_2O$  and

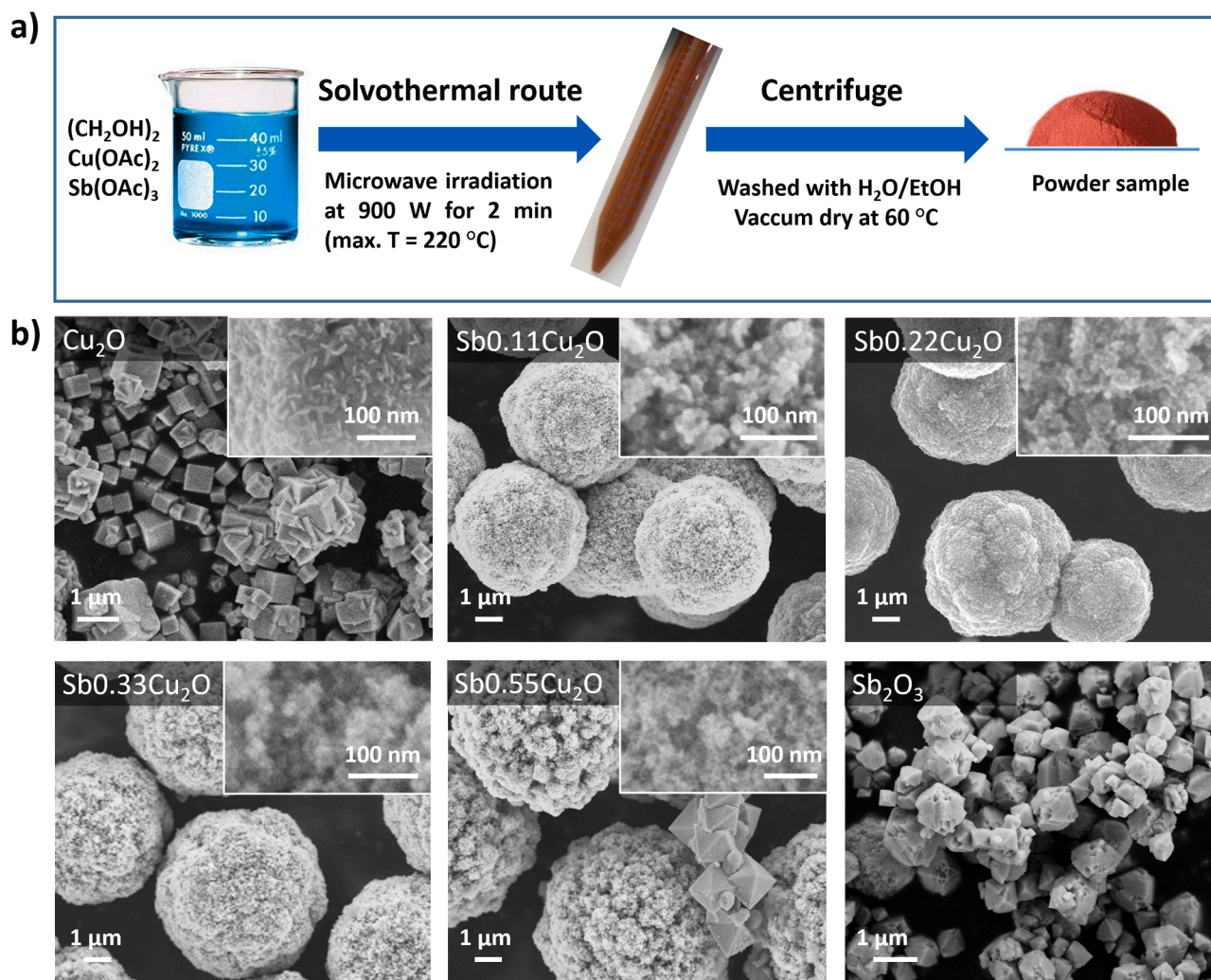


**Fig. 1.** (a) Schematic of a typical synthesis process. FESEM images of the materials: (b)  $Cu_2O$ , (c)  $Sb_{0.11}Cu_2O$ , (d)  $Sb_{0.22}Cu_2O$ , (e)  $Sb_{0.33}Cu_2O$ , (f)  $Sb_{0.55}Cu_2O$  and (g)  $Sb_2O_3$ .



Sb<sub>0.55</sub>Cu<sub>2</sub>O samples are estimated as  $15 \pm 2$  nm,  $12 \pm 4$  nm and  $14 \pm 1$  nm, respectively. In addition to Cu<sub>2</sub>O, the Sb<sub>0.55</sub>Cu<sub>2</sub>O sample also contains cubic Sb<sub>2</sub>O<sub>3</sub> crystalline phase with an estimated crystallite size of  $109 \pm 5$  nm, which is slightly smaller than those in the Sb<sub>2</sub>O<sub>3</sub> sample. The detailed XRD analysis unveils that the addition of Sb has dramatically reduced the crystallite size of the Cu<sub>2</sub>O phase and that its incorporation up to a high nominal content of 25 at% (Sb<sub>0.33</sub>Cu<sub>2</sub>O

sample) has not resulted in crystalline Sb species. It is further noticed that the lattice constant is slightly altered due to the Sb incorporation, with a percentage variation lower than 0.5% for the Sb-Cu<sub>2</sub>O samples with respect to the Cu<sub>2</sub>O sample (Table S2). Even though the insignificant variation in the lattice parameter, it is not ruled out that Sb could be successful incorporated into Cu<sub>2</sub>O crystal host at high concentrations, due to the similar radius size of Sb(III) with that of Cu(I) [49–51].

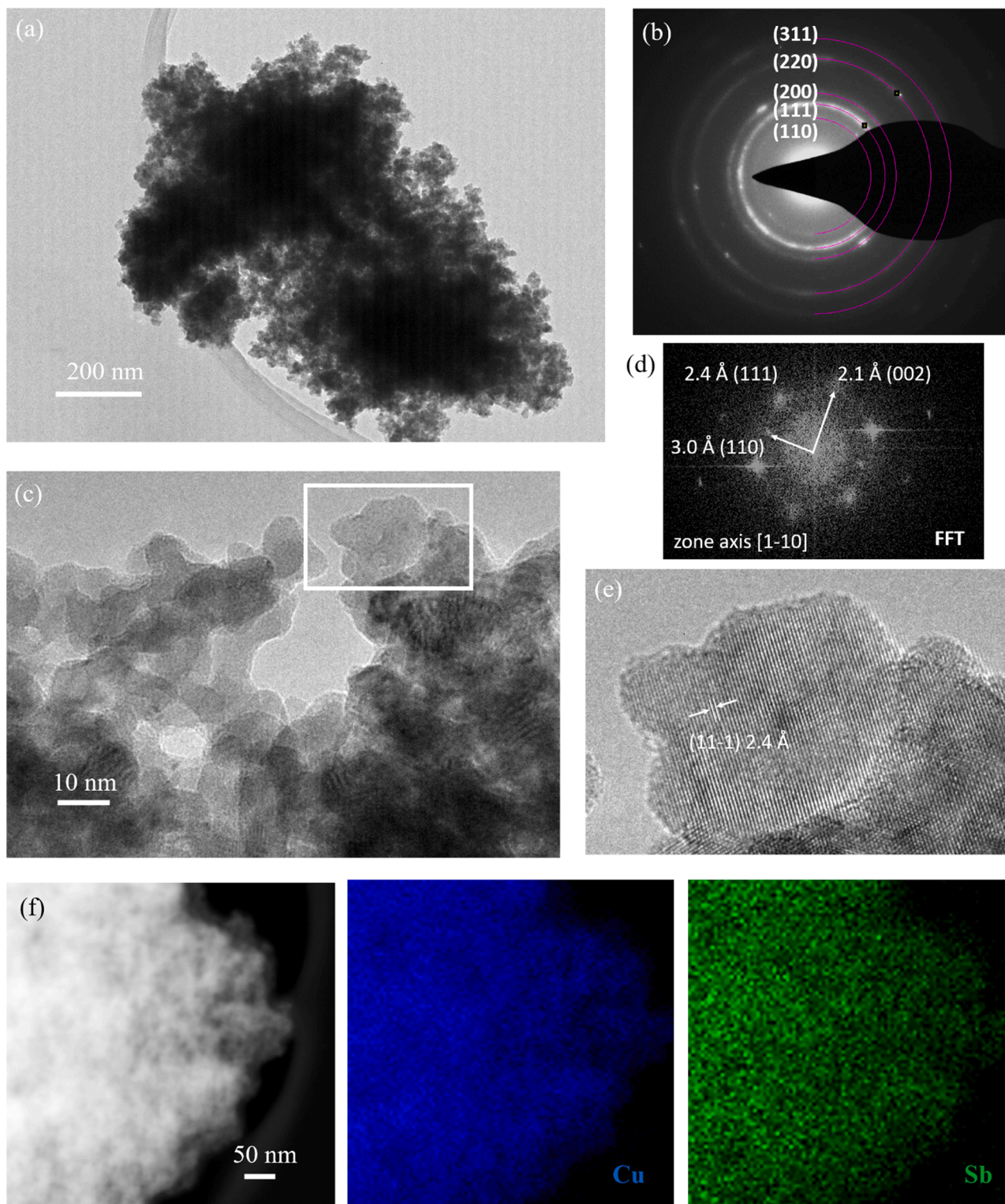


**Fig. 2.** TEM characterization of the Sb<sub>0.22</sub>Cu<sub>2</sub>O sample: (a) low-magnification image with related (b) SAED pattern, (c) HR investigation of the highlighted region with the FFT (d) of the corresponding HRTEM image (e). (f) HAADF STEM image alongside EDX elemental maps for Cu and Sb elements.



The uniform incorporation of Sb in the  $\text{Cu}_2\text{O}$  crystalline phase has further been investigated for the  $\text{Sb}_{0.22}\text{Cu}_2\text{O}$  sample by means of TEM, through Selected Area Electron Diffraction (SAED), high-resolution (HR) TEM imaging and EDX elemental maps. Since the micrometric spheres of  $\text{Sb}_{0.22}\text{Cu}_2\text{O}$  are not electron transparent, the powder sample was sonicated for 30 min before TEM analysis in order to detach some nanometric particles which constitute the micro-spheres. Representative results for the TEM characterization are provided in Fig. 2. The sonication procedure allows to obtain electron-transparent regions (Fig. 2a) from which it is possible to acquire SAED patterns, such as the one shown in Fig. 2b. The presence of diffraction rings is characteristic of the polycrystalline nature of the material and careful analysis of the diffraction pattern (Table S3) confirms that the crystalline phase is  $\text{Cu}_2\text{O}$ , without any signature of  $\text{Sb}_2\text{O}_3$  phase, in accordance with XRD results. Nanoscale structural analysis by HRTEM (Fig. 2c-e) shows that  $\text{Cu}_2\text{O}$  crystallites have a characteristic size in accordance with the one ( $15 \pm 2$  nm) obtained from the Rietveld analysis of XRD data. Moreover, analysis of HRTEM images confirms the absence of  $\text{Sb}_2\text{O}_3$  phase and suggests the incorporation of Sb in the  $\text{Cu}_2\text{O}$  crystalline phase. Further indication is obtained by EDX elemental mapping. Fig. 2f presents a High-Angle Annular Dark-Field (HAADF) Scanning Transmission Electron Microscopy (STEM) image, coupled with its corresponding elemental Cu and Sb maps. Since the elemental contrast in both EDX maps correlates with the atomic-number contrast (Z-contrast) of the HAADF image, it is reasonable to assume that Sb is uniformly incorporated into the  $\text{Cu}_2\text{O}$  nanostructures at the nanoscale. It is important to notice that elemental distribution (EDX maps) and structural information (HRTEM analysis at the edges) were also obtained for the micro-spheres (Fig. S3) and these results are in accordance with the ones obtained from the electron-transparent regions. Hence, it is possible to state the Sb distribution is homogeneous at both nanometric and micrometric scales.

XPS measurements have been performed on the  $\text{Sb}_2\text{O}_3$ ,  $\text{Sb-Cu}_2\text{O}$  and  $\text{Cu}_2\text{O}$  samples to investigate the chemical composition of the surface. From the survey spectra, Cu, Sb, O and C are the main elements for all  $\text{Sb-Cu}_2\text{O}$  samples (Table S4). It is important to note that the Sb/Cu atomic ratios are close to the nominal ones, especially for the  $\text{Sb}_{0.11}\text{Cu}_2\text{O}$ ,  $\text{Sb}_{0.22}\text{Cu}_2\text{O}$  and  $\text{Sb}_{0.33}\text{Cu}_2\text{O}$  samples. Detailed information on the oxidation states of Sb and Cu elements on the  $\text{Sb}_{0.22}\text{Cu}_2\text{O}$  sample have been obtained from HR analysis (Fig. 3). In order to get information from the Sb3d doublet, we had to deconvolute its signal starting from Sb3d<sub>3/2</sub> peak, since the Sb3d<sub>5/2</sub> overlaps with O1s signal. Hence, the intensity and binding energy of Sb3d<sub>5/2</sub> peak have been set by the Sb3d<sub>3/2</sub> peak's position and intensity, according to the spin-orbit splitting ( $\Delta = 9.39$  eV) and ratio (0.7), and the remaining area in the Sb3d<sub>5/2</sub> peak is attributed to O 1s signal. As shown in Fig. 3a, the Sb3d doublet shows only one oxidation state related to Sb(III) [52]. O1s contribution has been deconvoluted in three peaks associated to metal

oxide (530 eV), C=O ( $\sim 531$  eV) and C-O ( $\sim 532$  eV), in which the latter two are due to ambient contamination (adsorbates). The Cu2p doublet represents always a tricky region to be analyzed, since Cu(I) and Cu(0) are commonly reported at the same binding energy, while Cu(II) is well recognizable due to the presence of its satellite between 940 and 945 eV. To overcome this issue, Auger CuLMM region has also been acquired to enable the calculation of the Auger parameter, which can help to understand the average Cu oxidation state. From the Cu2p<sub>3/2</sub> position (932.5 eV) and small satellite at 942 eV (Fig. 3b), we can appreciate the presence of main Cu(I) oxidation state with minor Cu(II) [53]. From the maximum position ( $E_K = 916.8$  eV) of the CuLMM peak (inset of Fig. 3b), an Auger parameter of 1848.8 eV is obtained (Table S5) and it is commonly attributed to Cu(I) [53], in accordance with the XRD and TEM analyses. Cu(II) is absent in the diffraction analyses, probably due to their low amount or their amorphous phase [54,55]. The oxides in the upmost layer can be formed due to the exposure to atmosphere [54,56]. Other  $\text{Sb-Cu}_2\text{O}$  samples possess similar surface chemical characteristics with respect to the  $\text{Sb}_{0.22}\text{Cu}_2\text{O}$ , except that all these samples have notable differences in the surface atomic ratio of Sb/Cu, as shown in Table S4 and S5. With raising the ratio of the Sb/Cu salts in the precursor solution, the Sb percentage on the  $\text{Sb-Cu}_2\text{O}$  surface increases and the Sb content quantified by the inductively coupled plasma optical emission spectroscopy (ICP-OES) analysis rises as well (Table S6). The mono-metallic samples,  $\text{Cu}_2\text{O}$  and  $\text{Sb}_2\text{O}_3$ , are also analyzed (Fig. S4 and S5). The surface of  $\text{Cu}_2\text{O}$  sample is rich of Cu (II) and thus is more oxidized compared to that of  $\text{Sb-Cu}_2\text{O}$  samples, while the Sb element on the  $\text{Sb}_2\text{O}_3$  sample shows Sb(III) as the only oxidation state as observed on the  $\text{Sb-Cu}_2\text{O}$  samples.

### 3.2. Comparison of $\text{CO}_2\text{RR}$ activity on $\text{Sb-Cu}_2\text{O}$ derived catalysts

Voltammetric study has been performed at various electrodes in a  $\text{CO}_2$ -saturated 0.1 M  $\text{KHCO}_3$  electrolyte in order to study the electrochemical characteristics of the materials. Unless otherwise specified, all potentials refer to the RHE in this work. From cyclic voltammograms in Fig. S6a and S6b, the electrodes with  $\text{Cu}_2\text{O}$  and  $\text{Sb}_2\text{O}_3$  show characteristic redox peaks of Cu and Sb species, respectively. All electrodes with  $\text{Sb-Cu}_2\text{O}$  show a cathodic peak attributed to the reduction of Sb species, and this peak increases in intensity from the electrode with  $\text{Sb}_{0.11}\text{Cu}_2\text{O}$  to that with  $\text{Sb}_{0.55}\text{Cu}_2\text{O}$  (Fig. S6c). On contrast, the redox peak of Cu species at high potential range shows an opposite trend. This outcome is in accordance with the surface composition of the materials, that is, Sb increases and Cu decreases from  $\text{Sb}_{0.11}\text{Cu}_2\text{O}$  to  $\text{Sb}_{0.55}\text{Cu}_2\text{O}$ . The reduction peaks of Sb and Cu cations indicate that both Cu and Sb oxides are (partially) reduced at potentials more positive than those where the  $\text{CO}_2\text{RR}$  experiments were conducted in this work ( $\leq -0.4$  V). Hence, under the  $\text{CO}_2\text{RR}$  conditions, the  $\text{Sb}_2\text{O}_3$ ,  $\text{Cu}_2\text{O}$  and  $\text{Sb-Cu}_2\text{O}$  ( $\text{SbxCu}_2\text{O}$ ) materials are restructured to form real catalysts, and the electrodes

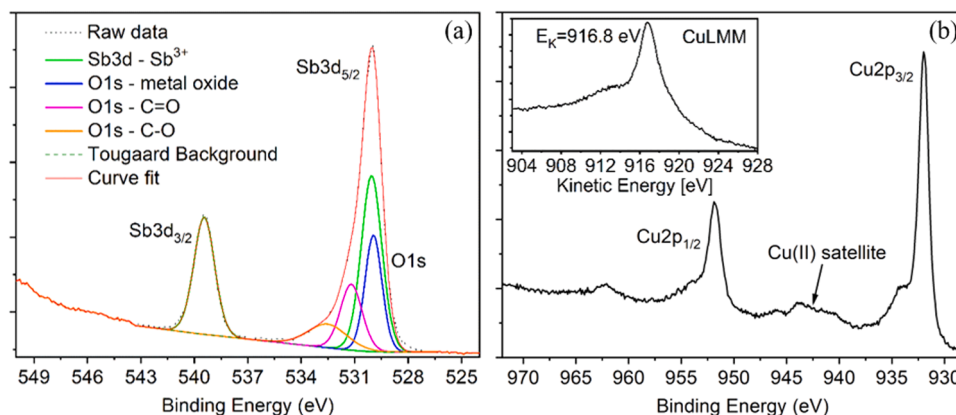


Fig. 3. XPS spectra of  $\text{Sb}_{0.22}\text{Cu}_2\text{O}$  sample: (a) HR XPS analysis of Sb element and (b) Cu2p doublet region acquired in HR mode and Auger CuLMM region in inset.

prepared with these materials are named Sb, Cu and Sb-Cu (SbxCu), respectively.

Fig. S6d shows the linear sweep voltammograms of various electrodes in the potential range where the CO<sub>2</sub>RR and its competing HER occur. All Sb-Cu electrodes display much lower onset potentials compared to the Cu one and they show much smaller current density with respect to the Sb electrode at low potentials ( $< -0.85$  V), demonstrating notable differences among the bimetallic and monometallic electrodes. Since the current normalized by geometric surface area of the electrode does not reflect the activity of the catalyst, we calculated the current normalized by the electrochemically active surface area (ECSA), as detailed in Table S7 and Fig. S7. As shown in Fig. S6e, the activity of these catalysts toward the reduction reactions follows a trend,  $\text{Cu} > \text{Sb0.11Cu} > \text{Sb0.22Cu} > \text{Sb0.33Cu} \approx \text{Sb0.55Cu}$ , at potentials lower than  $-0.55$  V. It is clear that addition of Sb decreases the overall activity of Cu catalyst toward the reduction reactions and an increase in the Sb content leads to a decrease in the activity of the Sb-Cu catalyst. The Sb catalyst shows slow activity at potentials higher than  $-0.75$  V and displays a fast increase in activity with lowering the potential in the more negative potential range. With respect to the Sb, the Sb-Cu catalysts show similar onset potentials but much lower activity in the low potential range ( $< -0.9$  V). This outcome implies that the Sb-Cu catalysts are also distinct from the Sb one toward the reduction reactions.

In order to understand the differences in the activity and selectivity among the Cu, Sb-Cu and Sb catalysts for the CO<sub>2</sub>RR, CA measurements were carried out in a three-electrode H-type cell (Fig. S1a) in a CO<sub>2</sub>-saturated 0.1 M KHCO<sub>3</sub> solution. Typical i-t curves and product analyses are shown in Fig. S8. Various electrodes are compared in Figs. 4a and 4b at  $-0.8$  V and  $-1.0$  V, respectively, in terms of both selectivity and geometric activity. The Cu electrode has poor selectivity for the CO<sub>2</sub>RR, with FE<sub>CO</sub> below 10% and FE<sub>HCOOH</sub> below 6% at both potentials. In contrast, at the Sb electrode, the HCOOH selectivity reaches a considerable value of 40% at  $-0.8$  V and it becomes less significant at  $-1.0$  V, while no trace of CO is detected at both potentials. Differing from the Cu

and Sb electrodes, the Sb-Cu ones mainly produce CO with minor HCOOH. Particularly, the Sb0.22Cu and Sb0.33Cu demonstrate a good selectivity for CO and relatively high geometric current densities at both potentials. The ECSA-normalized current densities on each electrode at  $-0.8$  V and  $-1.0$  V are shown in Figs. 4c and 4d, respectively. The Cu catalyst has much higher activity for the H<sub>2</sub> formation compared to that for CO and HCOOH formation, as evidenced by a normalized partial current density for H<sub>2</sub> 10–20 times larger than those for the latter two. With addition of 9.6 at% of Sb (Sb0.11Cu sample), the formation of both H<sub>2</sub> and HCOOH is dramatically suppressed, while the CO formation is impressively boosted. With respect to the Cu catalyst, the Sb0.11Cu reduces the activity for H<sub>2</sub> formation by 15 times at  $-0.8$  V and by 6 times at  $-1.0$  V, while it increases the activity for CO formation by 4–5 times. A further increase of Sb content leads to declined activity for CO formation but sustained inhibition of both HCOOH and H<sub>2</sub> formation at the Sb0.22Cu and Sb0.33Cu catalysts. Concerning the total activity for both CO<sub>2</sub>RR and HER, with respect to the Cu catalyst, 9.6 at% of Sb addition leads to a significant decrease of 50–60% and further Sb addition results in a tremendous decrease of 75%, as also observed from the linear sweep voltammetry analysis. The Sb0.11Cu catalyst shows the highest activity for CO formation (Figs. 4c and 4d), while its electrode shows much lower geometric activity than the Sb0.22Cu and Sb0.33Cu electrodes (Figs. 4a and 4b), due to the much smaller ECSA of the former (Table S7). From comparison, the Sb0.22Cu electrode demonstrates the best selectivity and highest geometric current densities for CO formation.

### 3.3. CO<sub>2</sub> electrolysis on the Sb0.22Cu sample

Further investigations have been performed at the Sb0.22Cu electrode in a wide potential range from  $-0.5$  V to  $-1.2$  V in 0.1 M KHCO<sub>3</sub> electrolyte. As shown in Fig. 5a, the Sb0.22Cu electrode exhibits good potential for converting CO<sub>2</sub> to CO. It is the main product from the CO<sub>2</sub>RR and becomes dominant at potentials lower than  $-0.5$  V. The CO selectivity is characterized by an FE value of about 85% at  $-0.6$  V

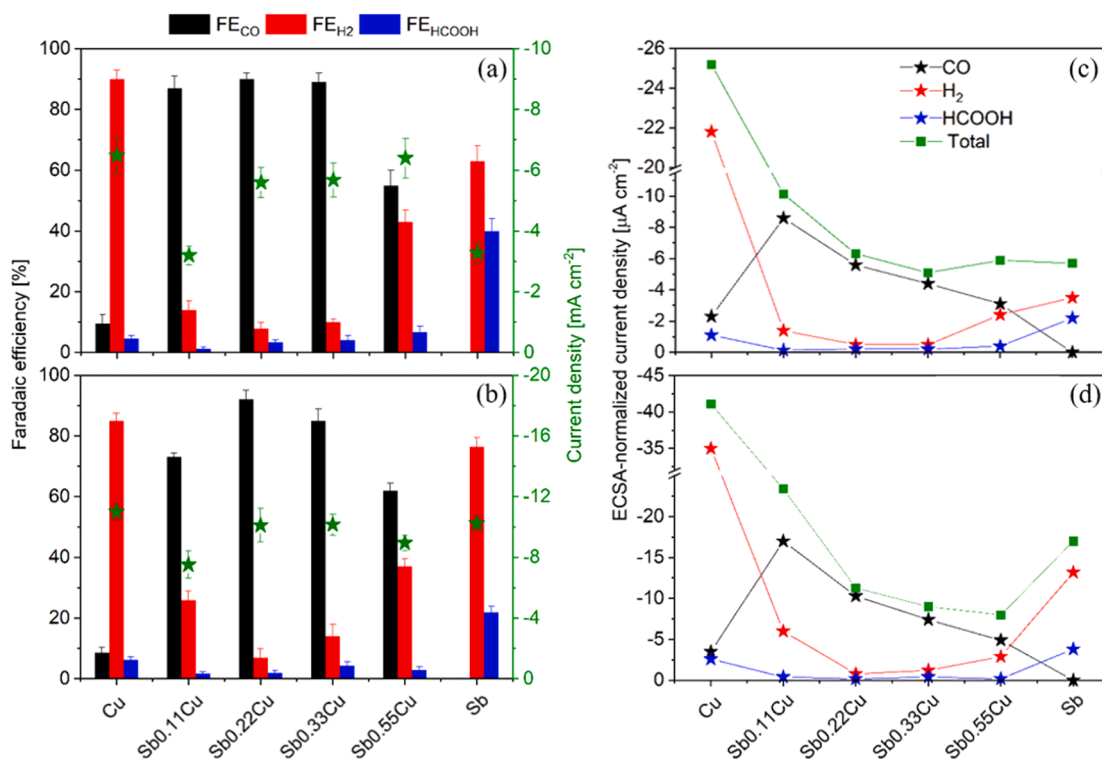


**Fig. 4.** FE values and geometric current densities at various electrodes in 0.1 M KHCO<sub>3</sub> electrolyte under applied potential: (a)  $-0.8$  V and (b)  $-1.0$  V. ECSA-normalized partial and total current densities at various electrodes under applied potential: (c)  $-0.8$  V and (d)  $-1.0$  V.



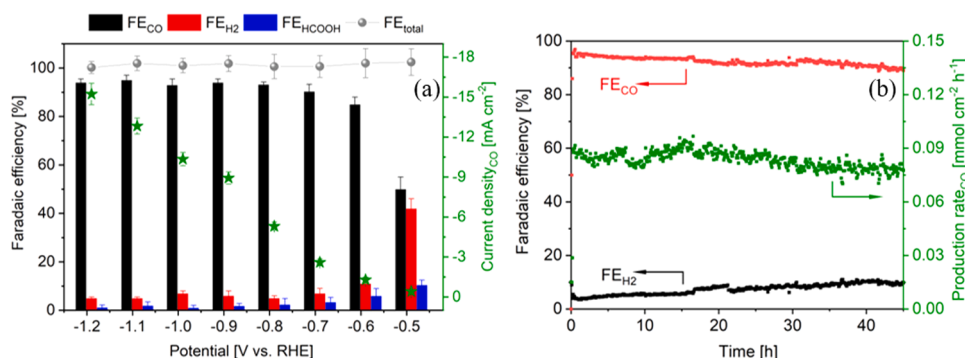


**Fig. 5.** CO<sub>2</sub>RR on the Sb<sub>0.22</sub>Cu electrode in 0.1 M KHCO<sub>3</sub> electrolyte: (a) FE values for various products and current densities for CO formation at various applied potentials and (b) FE values for main products and production rate of CO during a long-term stability test at  $-0.8$  V.

(overpotential  $\eta = 490$  mV) and enhanced up to 90–95% from  $-0.7$  V to  $-1.2$  V ( $\eta = 690$ – $990$  mV). The  $\text{FE}_{\text{H}_2}$  maintains at low values ( $\leq 7\%$ ) from  $-0.7$  V to  $-1.2$  V and the  $\text{FE}_{\text{HCOOH}}$  formation occupies even lower FE (1–3%) at potentials more negative than  $-0.7$  V. The current density for CO formation is  $0.41 \text{ mA cm}^{-2}$  at  $-0.5$  V and it rapidly increases to  $15.2 \text{ mA cm}^{-2}$  at  $-1.2$  V. The obtained current densities are in the range of reported values in aqueous CO<sub>2</sub> system with similar electrolytes and the low values are attributed to the limited reducible CO<sub>2</sub> in aqueous electrolyte [57,58]. The long-term stability of the Sb<sub>0.22</sub>Cu electrode was further evaluated at  $-0.8$  V, as shown in Fig. 5b. During a 45-hour test, the production rate of CO shows a good retention of about 93%, decreasing from about  $0.086 \text{ mmol cm}^{-2} \text{ h}^{-1}$  at the first hours to approximately  $0.08 \text{ mmol cm}^{-2} \text{ h}^{-1}$  at the end. The  $\text{FE}_{\text{CO}}$  displays a similar trend and it decreased from 94% to 90% during the test. The good retention of the electrode indicates satisfactory durability of Sb<sub>0.22</sub>Cu under working conditions.

The performance of the Sb<sub>0.22</sub>Cu electrode for the CO<sub>2</sub>RR to CO has been studied in KHCO<sub>3</sub> electrolyte with various concentrations. As shown in Fig. 6a–c, the selectivity of the electrode is slightly affected by the KHCO<sub>3</sub> concentration from  $-0.6$  V to  $-0.9$  V and excellent FE

values (90–96%) for CO formation are obtained in all electrolytes. At potentials higher than  $-0.6$  V, the CO selectivity is slightly enhanced as increasing the KHCO<sub>3</sub> concentration until 1.0 M, while the CO formation is less favored at potentials lower than  $-0.9$  V when increasing the KHCO<sub>3</sub> concentration to 2.0 M. In contrast to the selectivity, the electrode activity is dramatically influenced by the electrolyte composition and it is significantly boosted by increasing the KHCO<sub>3</sub> concentration at each potential. In 2.0 M KHCO<sub>3</sub> electrolyte, the Sb<sub>0.22</sub>Cu electrode achieves CO partial current densities of  $37.3 \text{ mA cm}^{-2}$  and  $74.0 \text{ mA cm}^{-2}$  at  $-0.8$  V and  $-1.2$  V, respectively. The Sb<sub>0.22</sub>Cu electrode was also tested in KOH electrolyte with a flow reactor (Fig. S1b) and it can produce a CO partial current density of approximately  $60 \text{ mA cm}^{-2}$  at  $-0.8$  V (Fig. S9), which is even superior to the highest value obtained in KHCO<sub>3</sub> electrolyte at the same potential, implying that this electrode could be suitable to be applied in a wide range of electrolytes. Fig. 6d–f show the selectivity of the main gas products and CO partial current density on the Sb<sub>0.22</sub>Cu electrode at  $-0.8$  V in KHCO<sub>3</sub> electrolyte during prolonged tests. It is demonstrated that the electrode possesses good stability in terms of selectivity and activity in KHCO<sub>3</sub> electrolyte with various concentrations. Together

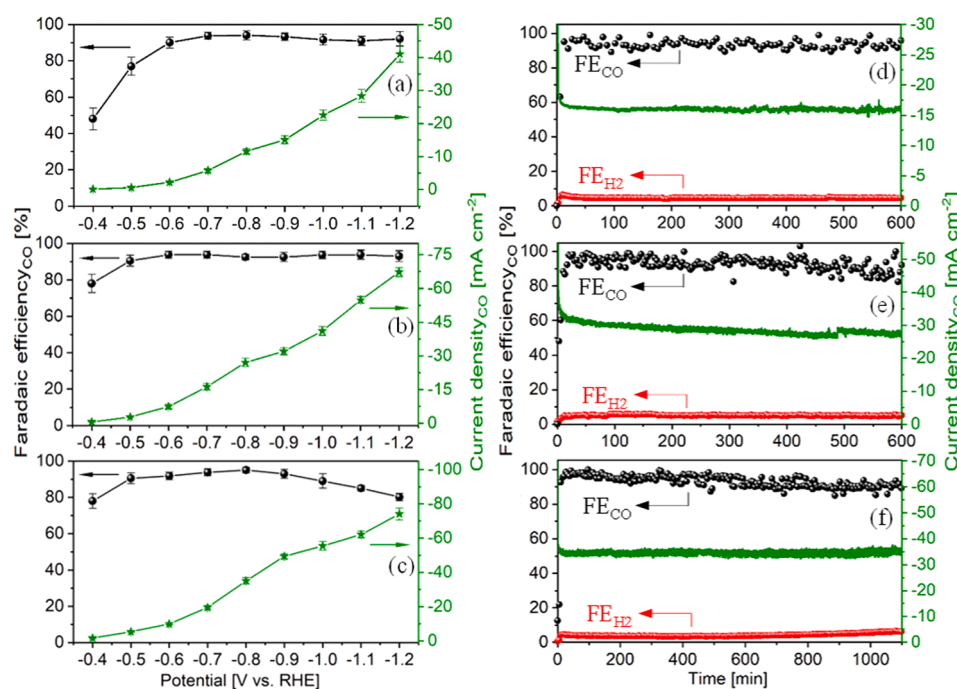


**Fig. 6.** CO<sub>2</sub>RR on the Sb<sub>0.22</sub>Cu electrode: FE values and current densities for CO formation at various applied potential in KHCO<sub>3</sub> electrolyte with different concentrations (a) 0.5 M, (b) 1.0 M and (c) 2.0 M; FE values for main gas products and current densities for CO formation at  $-0.8$  V in KHCO<sub>3</sub> electrolyte with various concentrations (d) 0.5 M, (e) 1.0 M and (f) 2.0 M.

with the prolonged tests at  $-1.2$  V (Fig. S10), it is possible to state that the Sb0.22Cu electrode possesses good durability at various current densities ranging from  $5.6 \text{ mA cm}^{-2}$  to  $100 \text{ mA cm}^{-2}$ . By comparison with other reported CO-selective catalysts (Table S8), it is evident that the herein proposed Sb-Cu material shows outstanding performance for the  $\text{CO}_2\text{RR}$  to CO in terms of selectivity, activity and durability.

Finally, to study the effect of  $[\text{HCO}_3^-]$ , we performed the  $\text{CO}_2$  electrolysis at a constant potential of  $-0.8$  V in electrolytes with various  $[\text{HCO}_3^-]$  ranging from  $0.05$  to  $2.0$  M. As shown in Fig. 7a, the  $\text{CO}_2\text{RR}$  to CO rate increases with increasing the  $\text{HCO}_3^-$  concentration. A plot of  $\log(j_{\text{CO}})$  in function of  $\log([\text{HCO}_3^-]_{\text{bulk}})$  shows a slope of  $0.8$ , indicating approximately first-order dependence of the reaction rate on the  $[\text{HCO}_3^-]_{\text{bulk}}$ . Based on this outcome, it is widely accepted that the  $\text{HCO}_3^-$  ions act as proton donors and participate in the  $\text{CO}_2\text{RR}$  to CO [59–62]. However, Dunwell et al. [63] found that replacing the  $\text{HCO}_3^-$  with other similar proton donors such as  $[\text{HPO}_4^{2-}]$  fails to maintain the first-order dependence of the reaction rate on the  $[\text{HPO}_4^{2-}]$ , suggesting that the primary role of the  $\text{HCO}_3^-$  ions could be not proton donor. They proposed that  $\text{HCO}_3^-$  enhances the  $\text{CO}_2\text{RR}$  to CO rate by increasing the availability of  $\text{CO}_2$  near the electrode surface ( $[\text{CO}_2]_{\text{local}}$ ) through rapid equilibrium between  $\text{HCO}_3^-$  and dissolved  $\text{CO}_2$ . To correlate  $[\text{CO}_2]_{\text{local}}$  and  $[\text{HCO}_3^-]_{\text{local}}$  with  $[\text{HCO}_3^-]_{\text{bulk}}$ , we employed a diffusion model reported in our previous work [35], taking into consideration the bubble-induced mass transport near the electrode. The model is based on fitting the experimental data reported in Figs. 5a and 6a–c. The evaluation of the size of gas bubbles is the basic step of the bubble-induced mass transport modelling. The bubble aperture diameters able to give the best fits between the experimental data and the calculated CO partial current density-potential curves are found to be

equal to  $500 \mu\text{m}$ ,  $75 \mu\text{m}$ ,  $20 \mu\text{m}$  and  $10 \mu\text{m}$  in  $0.1$  M,  $0.5$  M,  $1.0$  M and  $2.0$  M  $\text{KHCO}_3$  electrolyte, respectively, as shown in Fig. S11. The bubble-induced mass transport model then proceeded with the values of the bubble aperture diameters, as detailed in our previous work [35]. As shown in Fig. S12, the  $[\text{CO}_2]_{\text{local}}$  quickly decreases with lowering the applied potentials in each electrolyte and it increases as raising the  $[\text{HCO}_3^-]_{\text{bulk}}$  at the same potential in the high overpotential range ( $-1.0$  to  $-1.2$  V). In contrast, the  $[\text{HCO}_3^-]_{\text{local}}$  shows a slower decrease while negatively shifting the potential and it remains significantly higher in larger  $[\text{HCO}_3^-]_{\text{bulk}}$  solution (Fig. S13). The  $[\text{CO}_2]_{\text{local}}$  and  $[\text{HCO}_3^-]_{\text{local}}$  are plotted as function of  $[\text{HCO}_3^-]_{\text{bulk}}$  at  $-1.2$  V where the reaction rate is the highest in each  $[\text{HCO}_3^-]_{\text{bulk}}$  electrolyte (Fig. 7b). It is clear that a higher  $[\text{HCO}_3^-]_{\text{bulk}}$  dramatically enhances both  $[\text{CO}_2]_{\text{local}}$  and  $[\text{HCO}_3^-]_{\text{local}}$ . When plotting  $\log([\text{CO}_2]_{\text{local}})$  in function of  $\log([\text{HCO}_3^-]_{\text{local}})$ , a slope of  $1.0$  is obtained, as shown in Fig. 7c. The first-order dependence of  $[\text{CO}_2]_{\text{local}}$  on  $[\text{HCO}_3^-]_{\text{local}}$  reflects significant relevance between reducible  $\text{CO}_2$  and  $\text{HCO}_3^-$  ions, indicating that the enhancement of the  $\text{CO}_2\text{RR}$  to CO rate by increasing  $[\text{HCO}_3^-]_{\text{bulk}}$  is likely attributed to the improvement of  $\text{CO}_2$  availability near the electrode surface.

### 3.4. Characterizations of the tested electrodes

Further analyses have been performed on the tested Sb, Cu and Sb0.22Cu electrodes in order to investigate the restructuring of the materials. XRD analysis shows that metallic Cu and  $\text{Cu}_2\text{O}$  are observed in the reduced Cu and Sb0.22Cu electrodes (Fig. S14). No evidence of crystalline Sb species is observed in the Sb0.22Cu electrode, while only diffraction peaks associated to metallic Sb appear in the Sb electrode. XPS analysis evidences that only Cu(0) and Sb(III) exist on the surface of

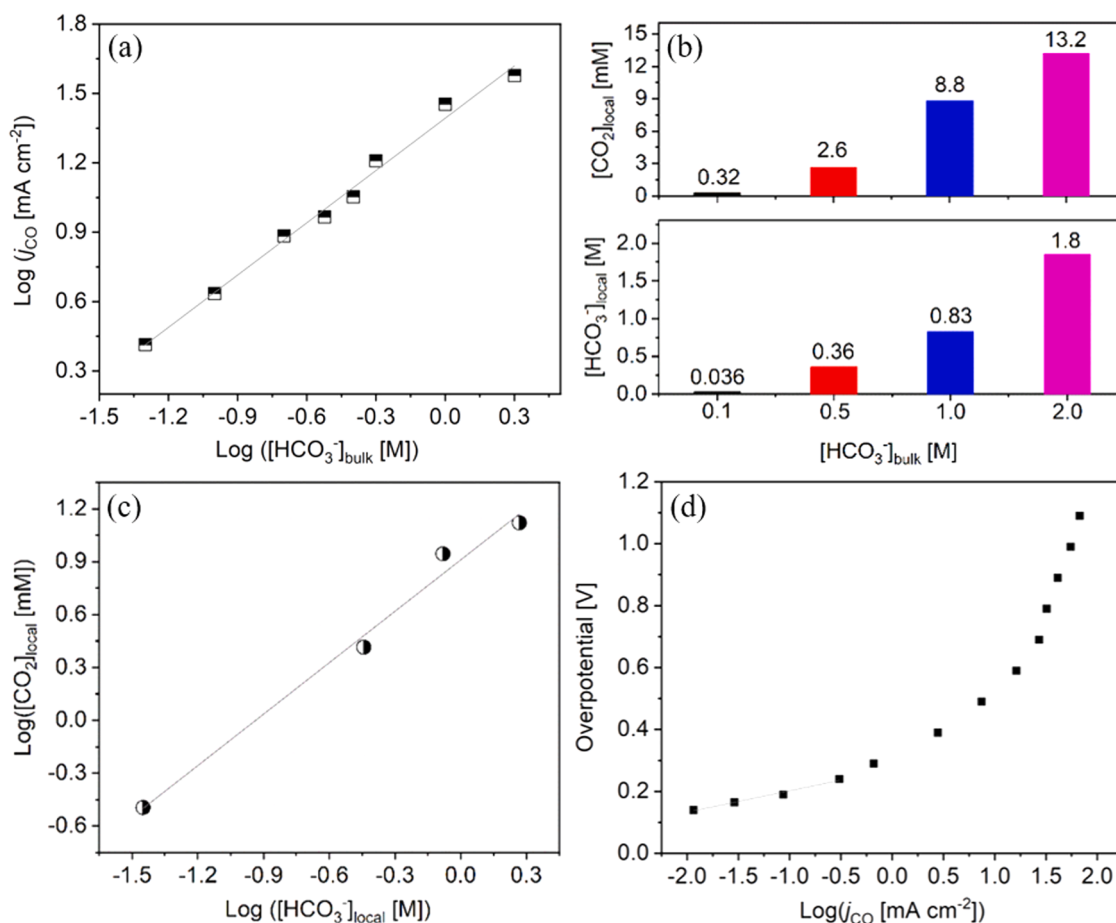


**Fig. 7.** Dependence of CO formation rate on the bulk  $\text{HCO}_3^-$  concentration at  $-0.8$  V (a),  $[\text{CO}_2]_{\text{local}}$  and  $[\text{HCO}_3^-]_{\text{local}}$  as function of  $[\text{HCO}_3^-]_{\text{bulk}}$  at  $-1.2$  V (b), dependence of  $[\text{CO}_2]_{\text{local}}$  on  $[\text{HCO}_3^-]_{\text{local}}$  at  $-1.2$  V (c) and Tafel plot at Sb0.22Cu electrode in  $1.0$  M  $\text{KHCO}_3$  electrolyte (d).



the Sb<sub>0.22</sub>Cu electrode (Fig. S15a-c), and Sb(III) is partially reduced to Sb(0) on the surface of the Sb electrode (Fig. S15d). Based on these results, it is believed that the small quantity of Cu<sub>2</sub>O detected by XRD can be formed during the sample preparation and the ex-situ measurement in air, and Cu oxides are fully reduced to metallic Cu under negative potentials for the CO<sub>2</sub>RR, which is consistent with the widely reported results obtained by in-situ/operando techniques [64–68]. Regarding the Sb species under the CO<sub>2</sub>RR conditions, it is convincing that Sb(0) is formed, while it is impossible to exclude the coexistence of cationic Sb with the herein used ex-situ techniques.

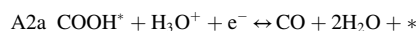
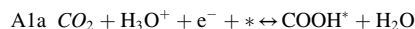
### 3.5. Mechanism study of the CO<sub>2</sub>RR to CO on Sb-Cu materials

To elucidate the mechanism of CO<sub>2</sub>RR on Sb-Cu samples, it is important to primarily determine the geometry of the most stable catalyst surface, on which the electrochemical reactions are likely to take place. Thermodynamic data and above-mentioned discussion suggest that Cu(I) in the as-synthesized catalyst is reduced to Cu(0) under catalytic conditions. Among the possible Cu surfaces, we focused on terraced Cu(111), the most stable surface exposed by pristine metallic Cu, and on Cu(211), as representative of higher energy stepped structure. By means of DFT calculations, we found that for both (111) and (211) terminations, Sb atoms prefer to segregate toward the outer surface layers since the configuration containing the dopant atom in the top surface layer is thermodynamically more stable compared to sub-surface positions (energy gain of 2.10 eV). Furthermore, the formation of Sb clusters on the surface is found to be thermodynamically unfavored, confirming the finding based on TEM and EDX maps analysis (Fig. 2). A combined DFT and CE approach was employed to predict the structural properties of Sb<sub>x</sub>Cu<sub>(1-x)</sub> alloys and to compare the stability of Sb<sub>x</sub>Cu<sub>(1-x)</sub>(111) and Sb<sub>x</sub>Cu<sub>(1-x)</sub>(211) surfaces. A null surface concentration ( $x = 0$ ) consists of pure Cu surfaces while a surface concentration  $x = 1$  corresponds to a Cu surface where all exposed Cu atoms are substituted by Sb atoms. Results of CE performed on both surfaces are plotted in Fig. S16, showing the DFT calculated surface formation energy  $\gamma_{form}$  used for the CE fitting together with the resulting predicted  $\gamma_{form}$  from the CE. The Cu(211) surface CE is plotted in blue, Cu(111) surface CE in red, and the dashed lines represent all the ground states throughout the phase diagram. From Fig. S16 it is possible to notice that as Sb is added to the Cu surface layer, the formation energy of the Sb<sub>x</sub>Cu<sub>(1-x)</sub>(111) surface increases monotonically, while formation energy of the Cu<sub>(1-x)</sub>Sb<sub>x</sub>(211) surface decreases, reaching a minimum at  $x = 0.5$ . The effect of Sb atoms is therefore the stabilization of the stepped (211) surface with respect to the flat (111). Moving from  $x = 0$  to  $x = 1$ , the most stable Sb<sub>x</sub>Cu<sub>(1-x)</sub> (211) surface structures consist of a progressive Sb substitution of Cu atoms starting from the edge of the steps in such a manner that each Sb first-neighbor site is occupied by a Cu atom, as shown in Figures 16b-c, confirming the Sb tendency to prefer undercoordinated positions. Sb atoms introduce distortions in the surface plane that alter the initial atomic arrangement and allow for outward relaxation of Sb atoms. In Sb<sub>x</sub>Cu<sub>(1-x)</sub>(211) structures with  $x \geq 0.5$  the surface reconstruction is such to expose Sb atoms only. As confirmed by the experiments, DFT calculations predict that Sb activity in the CO<sub>2</sub>RR is extremely low (see Supporting Information, Table S9), therefore high Sb concentrations ( $x \geq 0.5$ ) prevent the interactions between reactants and Cu active sites, thus hindering the electrocatalytic performances. For these reasons, we argue that the most likely surface concentration values of the active catalysts will fall around intermediate values ( $0.2 < x < 0.5$ ) at which the (211) surface is stabilized and not yet covered by a full Sb monolayer. In the study of the reaction mechanism, we considered the (211) surface at  $x = 0.33$ .

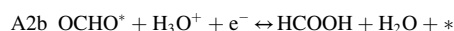
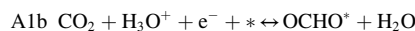
To enable the mechanism study, we then obtained the electrokinetic experimental data, thanks to the highly efficient and stable CO<sub>2</sub>RR to CO on the Sb<sub>0.22</sub>Cu electrode. Tafel analysis is considered one of the most important tools in the mechanism prediction, even though it has some limitations [69]. As shown in Fig. 7d, the Tafel plot is built by plotting

overpotential as function of CO partial current density ( $j_{CO}$ ) in logarithm scale. A Tafel slope of 69 mV dec<sup>-1</sup> is obtained at low overpotentials ( $\eta < 300$  mV), which is close to 56 mV dec<sup>-1</sup>, indicating a chemical step (e.g. proton transfer) as the rate-limiting step, following a first electron transfer or a first coupled electron-proton transfer. This outcome is in agreement with a recent work by Nørskov et al. [70], in which it is found that the electron transfer to adsorbed \*CO<sub>2</sub> is very facile and thus unlikely to be rate-determining in CO<sub>2</sub> adsorption.

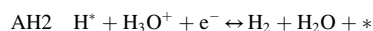
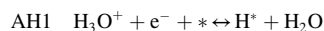
Assuming, then, an electron-proton transfer as the first step, CO<sub>2</sub>RR can proceed through the following steps, where hydronium ions in the solution are the proton sources



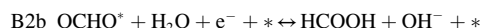
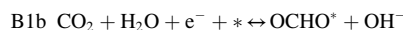
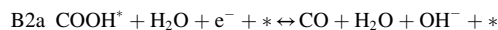
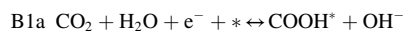
leading to CO production, or through



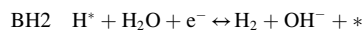
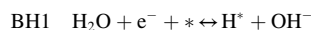
yielding formic acid. In competition to CO<sub>2</sub>RR, HER will unfold through the Volmer and Heyrovsky steps as



We do not consider the Tafel path for HER since on the catalyst surface H<sub>2</sub> dissociation is strongly disfavored due to the alternating presence of Cu and Sb atoms (H does not bind at Sb sites). CO<sub>2</sub>RR can also proceed with water as proton source, through the following steps



Similarly, HER will unfold via the alkaline Volmer-Heyrovsky mechanism



The free energy diagrams with activation barriers of CO<sub>2</sub>RR unfolding along the steps A (A1a+A2a toward CO and A1b+A2b toward HCOOH) and of HER along steps AH (AH1 +AH2), at pH= 6.8 and U= -0.5 V, are reported in Fig. 8a. The intermediate state geometries of \*COOH, \*OCHO and \*H are reported in Fig. 8c-d. Transition state geometries are reported in Fig. S17 for completeness. From Fig. 8a, it is possible to notice that step AH1 shows the lowest activation barrier and HER proceeds through proton consumption. When the applied potential is lowered and the reaction rate increases significantly, HER through AH1 and AH2 steps will be limited by proton diffusion from the bulk, determining an increase of local pH in the double layer [46,47,71,72]. The proton depletion in the double layer implies that reactions can proceed only from water splitting, unfolding along the B pathways. In Fig. 8b we report the free energy diagram with activation barriers of CO<sub>2</sub>RR following steps B (B1a+B2a toward CO and B1b+B2b toward HCOOH) and of HER along steps BH (BH1 +BH2) at U= -1.0 V and pH= 9. It is worth to note that the barrier of step BH1 is higher than the activation energy of step B1a, implying that HER is now disfavored with respect to CO<sub>2</sub>RR via the \*COOH intermediate. We also notice that the barriers of steps A1b and B1b are always higher than those of A1a and B1a, respectively, disfavoring HCOOH production. The interplay

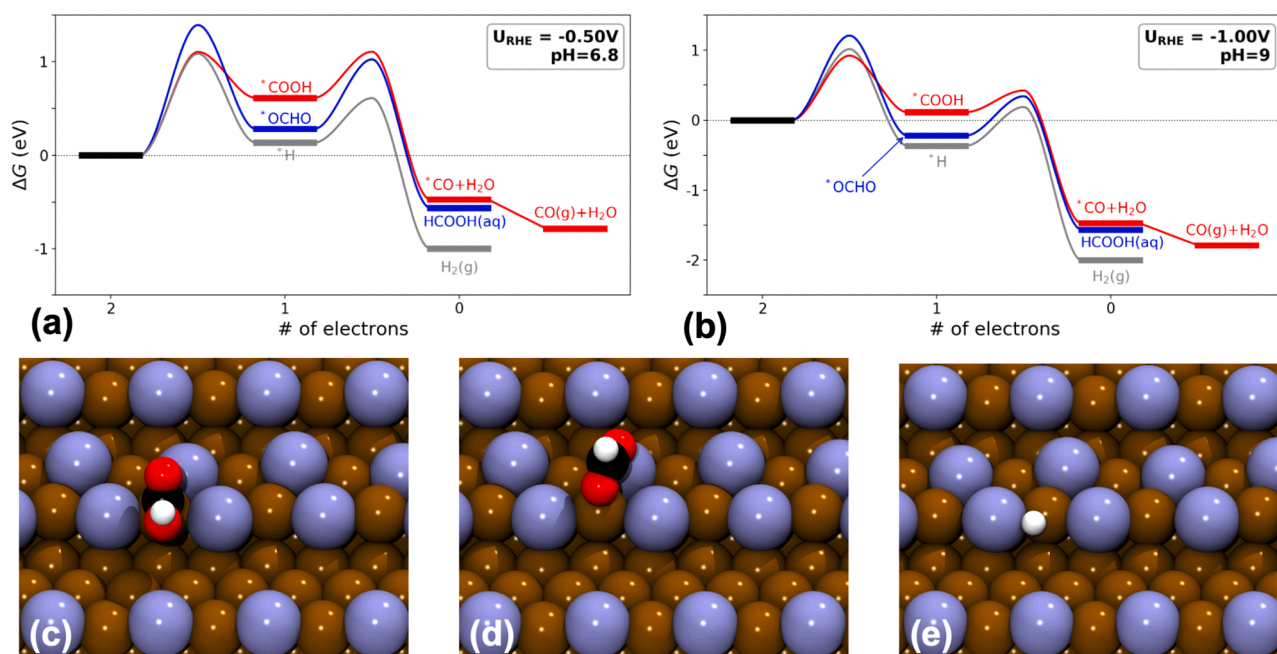


**Fig. 8.** Reaction energy diagrams for the dissociation of  $\text{CO}_2$  at  $-0.5\text{ V}$  vs RHE at pH 6.8 (a) and at  $-1.0\text{ V}$  vs RHE at pH 9 (b) on  $\text{Sb}_x\text{Cu}_{(1-x)}(211)$  surface with  $x = 0.33$ ; (red) electrochemical reduction to CO; (blue) electrochemical reduction to  $\text{HCOOH}$ ; (grey) hydrogen evolution reaction. Top view of intermediate state geometries for the adsorption of COOH (c), OCHO (d) and H (e) on  $\text{Sb}_x\text{Cu}_{(1-x)}(211)$  surface with  $x = 0.33$ . Cu atoms are represented in ochre, Sb atoms in iceblue, C atoms in black, O atoms in red and H in white.

between the kinetics of surface reactions, local pH and mass transport is therefore crucial to understand the mechanism of  $\text{CO}_2\text{RR}$ . At high potentials, HER is favored or competing with  $\text{CO}_2\text{RR}$ , since diffusion can keep up with proton consumption at the surface. At more negative potentials, acidic HER is hindered by proton depletion in the double layer, which, in turn, causes an increase of local pH and a switch to the alkaline mechanisms. In the latter case, our calculations unveil that the Cu-Sb stepped surface presents a kinetic barrier for step B1a on our catalyst lower than that for BH1, thus favoring the  $^*\text{COOH}$  intermediate. The surface morphology is also crucial in the following steps, since (see Fig. 8a,b), on this surface, adsorbed  $^*\text{CO}$ , resulted from  $^*\text{COOH}$  protonation, readily desorbs to  $\text{CO}(\text{g})$ , implying that electroreduction does not proceed further and the main product is indeed CO. Concisely, Sb plays a critically important role in the  $\text{CO}_2\text{RR}$  to CO process on the bimetallic catalyst by stabilizing stepped Cu surfaces selective for the reaction, lowering energy barriers for the formation of key intermediate and favouring the CO desorption instead of its further reduction. This explains the excellent performance of the optimal Sb-Cu catalyst for the desired reaction pathway.

#### 4. Conclusions

We have presented a Sb-Cu catalyst for effective  $\text{CO}_2\text{RR}$  to CO. The bimetallic material is successfully synthesized through a simple, green and upscalable route. Detailed analyses suggest that addition of Sb has promoted the formation of nanocrystalline  $\text{Cu}_2\text{O}$  particles with a narrow size distribution. The Sb element is homogeneously incorporated into the  $\text{Cu}_2\text{O}$  structure without formation of other crystalline phases at high contents, in accordance with the theoretical study that the formation of Sb clusters on the surface is thermodynamically unfavored. The optimized Sb-Cu bimetallic catalyst achieves excellent selectivity and high activity for the CO formation, and demonstrates good durability in a wide current density range. Detailed ab initio simulations firstly elucidate the origin of high performance of the Sb-Cu catalyst in the  $\text{CO}_2\text{RR}$  to CO process, giving new insights into the development of multimetallic catalysts for the  $\text{CO}_2$  conversion to a desired product. As the most important  $\text{C}_1$ -building block, CO has high relevance for the chemical

industry and is intensively used in large industrial processes such as Fischer-Tropsch synthesis of hydrocarbons and Monsanto/Cativa acetic acid synthesis. The herein proposed Sb-Cu material is low-cost and the fabrication method is environmentally friendly and energetically convenient, allowing their mass-scale production. Hence, it possesses good potential to be implemented in advanced  $\text{CO}_2$  electrolysis technologies such as gas diffusion electrodes and zero-gap electrolyzers to enable industrial scale  $\text{CO}_2$  conversion to CO. The present work highlights the versatility of Cu-based electrocatalysts and the importance of rational design of Cu multimetallic materials for the  $\text{CO}_2\text{RR}$  application.

#### CRediT authorship contribution statement

Dr. Zeng contributed to the conceptualization, the synthesis and electrochemical analyses. Dr. Re Fiorenza, Dr. Risplendi and Prof. Cicero contributed to the ab initio simulations. Dr. Castellino contributed to XPS investigation and the corresponding data analysis. Dr. Fontana contributed to FESEM and TEM investigations as well as XRD fitting. Dr. Sacco contributed to the EIS fitting and mass diffusion modelling. Dr. Farkhondehfar contributed to the HPLC analysis. Dr. Drago contributed to the ICP-OES analysis. Prof. Pirri contributed to the resources. All authors contributed to the composition of the manuscript.

#### Declaration of Competing Interest

The authors declare that they have no known competing financial interests or personal relationships that could have appeared to influence the work reported in this paper.

#### Appendix A. Supporting information

Supplementary data associated with this article can be found in the online version at [doi:10.1016/j.apcatb.2022.121089](https://doi.org/10.1016/j.apcatb.2022.121089).



## References

- [1] A. Sacco, R. Speranza, U. Savino, J. Zeng, M.A. Farkhondehfar, A. Lamberti, A. Chiodoni, C.F. Pirri, An Integrated Device for the Solar-Driven Electrochemical Conversion of CO<sub>2</sub> to CO, *ACS Sustain. Chem. Eng.* 8 (2020) 7563–7568.
- [2] T.N. Huan, D.A.D. Corte, S. Lamaison, D. Karapinar, L. Lutz, N. Menguy, M. Foldyna, S.-H. Turren-Cruz, A. Hagfeldt, F. Bella, M. Fontecave, V. Mougél, Low-cost high-efficiency system for solar-driven conversion of CO<sub>2</sub> to hydrocarbons, *PNAS* 116 (2019) 9735–9740.
- [3] J. Gurudayal, D.F. Bullock, C.M. Srankó, Y. Towle, M. Lum, M.C. Hettick, A. Scott, J. Ager Javey, Efficient solar-driven electrochemical CO<sub>2</sub> reduction to hydrocarbons and oxygenates, *Energy Environ. Sci.* 10 (2017) 2222–2230.
- [4] M. Schreier, F. Héroguel, L. Steier, S. Ahmad, J.S. Luterbacher, M.T. Mayer, J. Luo, M. Grätzel, Solar conversion of CO<sub>2</sub> to CO using Earth-abundant electrocatalysts prepared by atomic layer modification of CuO, *Nat. Energy* 2 (2017) 17087.
- [5] M. Schreier, L. Curvat, F. Giordano, L. Steier, A. Abate, S.M. Zakeeruddin, J. Luo, M.T. Mayer, M. Grätzel, Efficient photosynthesis of carbon monoxide from CO<sub>2</sub> using perovskite photovoltaics, *Nat. Commun.* 6 (2015) 7326.
- [6] Y. Hori, K. Kikuchi, S. Suzuki, PRODUCTION OF CO AND CH<sub>4</sub> IN ELECTROCHEMICAL REDUCTION OF CO<sub>2</sub> AT METAL ELECTRODES IN AQUEOUS HYDROGENCARBONATE SOLUTION, *Chem. Lett.* 14 (1985) 1695–1698.
- [7] Y. Hori, H. Wakebe, T. Tsukamoto, O. Koga, Electrocatalytic process of CO selectivity in electrochemical reduction of CO<sub>2</sub> at metal electrodes in aqueous media, *Electrochim. Acta* 39 (1994) 1833–1839.
- [8] A.A. Peterson, F. Abild-Pedersen, F. Studt, J. Rossmeisl, J.K. Nørskov, How copper catalyzes the electroreduction of carbon dioxide into hydrocarbon fuels, *Energy Environ. Sci.* 3 (2010) 1311–1315.
- [9] A.A. Peterson, J.K. Nørskov, Activity Descriptors for CO<sub>2</sub> Electroreduction to Methane on Transition-Metal Catalysts, *J. Phys. Chem. Lett.* 3 (2012) 251–258.
- [10] A. Bagger, W. Ju, A.S. Varela, P. Strasser, J. Rossmeisl, Electrochemical CO<sub>2</sub> Reduction: A Classification Problem, *ChemPhysChem* 18 (2017) 3266–3273.
- [11] S. Nitopi, E. Bertheussen, S.B. Scott, X. Liu, A.K. Engstfeld, S. Hørch, B. Seger, I.E. L. Stephens, K. Chan, C. Hahn, J.K. Nørskov, T.F. Jaramillo, I. Chorkendorff, Progress and Perspectives of Electrochemical CO<sub>2</sub> Reduction on Copper in Aqueous Electrolyte, *Chem. Rev.* 119 (2019) 7610–7672.
- [12] J. Zhao, S. Xue, J. Barber, Y. Zhou, J. Meng, X. Ke, An overview of Cu-based heterogeneous electrocatalysts for CO<sub>2</sub> reduction, *J. Mater. Chem. A* 8 (2020) 4700–4734.
- [13] S. Chu, X. Li, A.W. Robertson, Z. Sun, Electrocatalytic CO<sub>2</sub> Reduction to Ethylene over CeO<sub>2</sub>-Supported Cu Nanoparticles: Effect of Exposed Facets of CeO<sub>2</sub>, *Acta Phys. -Chim. Sin.* 37 (2021), 2009023.
- [14] P. De Luna, R. Quintero-Bermudez, C.-T. Dinh, M.B. Ross, O.S. Bushuyev, P. Todorović, T. Regier, S.O. Kelley, P. Yang, E.H. Sargent, Catalyst electroreduction controls morphology and oxidation state for selective carbon dioxide reduction, *Nat. Catal.* 1 (2018) 103–110.
- [15] L. Hao, Z. Sun, Metal Oxide-Based Materials for Electrochemical CO<sub>2</sub> Reduction, *Acta Phys. -Chim. Sin.* 37 (2021), 2009033.
- [16] C.W. Lee, K.D. Yang, D.-H. Nam, J.H. Jang, N.H. Cho, S.W. Im, K.T. Nam, Defining a Materials Database for the Design of Copper Binary Alloy Catalysts for Electrochemical CO<sub>2</sub> Conversion, *Adv. Mater.* 30 (2018), 1704717.
- [17] C.G. Morales-Guio, E.R. Cave, S.A. Nitopi, J.T. Feaster, L. Wang, K.P. Kuhl, A. Jackson, N.C. Johnson, D.N. Abram, T. Hatsukade, C. Hahn, T.F. Jaramillo, Improved CO<sub>2</sub> reduction activity towards C<sub>2+</sub> alcohols on a tandem gold on copper electrocatalyst, *Nat. Catal.* 1 (2018) 764–771.
- [18] S. Ajmal, Y. Yang, K. Li, M.A. Tahir, Y. Liu, T. Wang, A.-U.-R. Bacha, Y. Feng, Y. Deng, L. Zhang, Zinc-Modified Copper Catalyst for Efficient (Photo-) Electrochemical CO<sub>2</sub> Reduction with High Selectivity of HCOOH Production, *J. Phys. Chem. C* 123 (2019) 11555–11563.
- [19] T.T.H. Hoang, S. Verma, S. Ma, T.T. Fister, J. Timoshenko, A.I. Frenkel, P.J. A. Kenis, A.A. Gewirth, Nanoporous Copper-Silver Alloys by Additive-Controlled Electrodeposition for the Selective Electroreduction of CO<sub>2</sub> to Ethylene and Ethanol, *J. Am. Chem. Soc.* 140 (2018) 5791–5797.
- [20] W. Ren, X. Tan, J. Qu, S. Li, J. Li, X. Liu, S.P. Ringer, J.M. Cairney, K. Wang, S. C. Smith, C. Zhao, Isolated copper–tin atomic interfaces tuning electrocatalytic CO<sub>2</sub> conversion, *Nat. Commun.* 12 (2021), 1449.
- [21] W. Ju, J. Zeng, K. Bejtka, H. Ma, D. Rentsch, M. Castellino, A. Sacco, C.F. Pirri, C. Battaglia, Sn-Decorated Cu for Selective Electrochemical CO<sub>2</sub> to CO Conversion: Precision Architecture beyond Composition Design, *ACS Appl. Energy Mater.* 2 (2019) 867–872.
- [22] J. Zeng, K. Bejtka, W. Ju, M. Castellino, A. Chiodoni, A. Sacco, M.A. Farkhondehfar, S. Hernández, D. Rentsch, C. Battaglia, C.F. Pirri, Advanced Cu-Sn foam for selectively converting CO<sub>2</sub> to CO in aqueous solution, *Appl. Catal. B* 236 (2018) 475–482.
- [23] G.O. Barasa, T. Yu, X. Lu, X. Zhou, H. Wang, L. Qian, Y. Yu, L. Liu, P. Lei, Electrochemical training of nanoporous Cu-In catalysts for efficient CO<sub>2</sub>-to-CO conversion and high durability, *Electrochim. Acta* 295 (2019) 584–590.
- [24] Z.B. Hoffman, T.S. Gray, Y. Xu, Q. Lin, T.B. Gunnoe, G. Zangari, High Selectivity Towards Formate Production by Electrochemical Reduction of Carbon Dioxide at Copper-Bismuth Dendrites, *ChemSusChem* 12 (2019) 231–239.
- [25] X. Zhang, X. Sun, S.-X. Guo, A.M. Bond, J. Zhang, Formation of lattice-dislocated bismuth nanowires on copper foam for enhanced electrocatalytic CO<sub>2</sub> reduction at low overpotential, *Energy Environ. Sci.* 12 (2019) 1334–1340.
- [26] J. Medina-Ramos, R.C. Pupillo, T.P. Keane, J.L. DiMeglio, J. Rosenthal, Efficient Conversion of CO<sub>2</sub> to CO Using Tin and Other Inexpensive and Easily Prepared Post-Transition Metal Catalysts, *J. Am. Chem. Soc.* 137 (2015) 5021–5027.
- [27] F. Li, M. Xue, J. Li, X. Ma, L. Chen, X. Zhang, D.R. MacFarlane, J. Zhang, Unlocking the Electrocatalytic Activity of Antimony for CO<sub>2</sub> Reduction by Two-Dimensional Engineering of the Bulk Material, *Angew. Chem. Int. Ed.* 56 (2017) 14718–14722.
- [28] M. Jia, S. Hong, T.-S. Wu, X. Li, Y.-L. Soo, Z. Sun, Single Sb sites for efficient electrochemical CO<sub>2</sub> reduction, *Chem. Commun.* 55 (2019) 12024–12027.
- [29] Y. Li, S. Chu, H. Shen, Q. Xia, A.W. Robertson, J. Masa, U. Siddiqui, Z. Sun, Achieving Highly Selective Electrocatalytic CO<sub>2</sub> Reduction by Tuning CuO-Sb<sub>2</sub>O<sub>3</sub> Nanocomposites, *ACS Sustain. Chem. Eng.* 8 (2020) 4948–4954.
- [30] S. Mou, Y. Li, L. Yue, J. Liang, Y. Luo, Q. Liu, T. Li, S. Lu, A.M. Asiri, X. Xiong, D. Ma, X. Sun, Cu<sub>2</sub>Sb decorated Cu nanowire arrays for selective electrocatalytic CO<sub>2</sub> to CO conversion, *Nano Res* 14 (2021) 2831–2836.
- [31] Z. Zhang, Y. Yang, W. Li, W. Zhang, M. Liu, Z. Weng, S. Huo, J. Zhang, Boosting carbon monoxide production during CO<sub>2</sub> reduction reaction via Cu-Sb<sub>2</sub>O<sub>3</sub> interface cooperation, *J. Colloid Interface Sci.* 601 (2021) 661–668.
- [32] H. Li, T.-W. Jiang, X. Qin, J. Chen, X.-Y. Ma, K. Jiang, X.-G. Zhang, W.-B. Cai, Selective Reduction of CO<sub>2</sub> to CO on an Sb-Modified Cu Electrode: Spontaneous Fabrication and Physical Insight, *ACS Catal.* 11 (2021) 6846–6856.
- [33] S. Jia, Q. Zhu, H. Wu, M. Chu, S. Han, R. Feng, J. Tu, J. Zhai, B. Han, Efficient electrocatalytic reduction of carbon dioxide to ethylene on copper–antimony bimetallic alloy catalyst, *Chin. J. Catal.* 41 (2020) 1091–1098.
- [34] L. Lutterotti, S. Matthies, H.-R. Wenk, Combined texture and structure analysis of electrode limestone from time-of-flight neutron diffraction spectra, *J. Appl. Phys.* 81 (1997) 594–600.
- [35] A. Sacco, J. Zeng, K. Bejtka, A. Chiodoni, Modeling of gas bubble-induced mass transport in the electrochemical reduction of carbon dioxide on nanostructured electrodes, *J. Catal.* 372 (2019) 39–48.
- [36] N. Gupta, M. Gattrell, B. MacDougall, Calculation for the cathode surface concentrations in the electrochemical reduction of CO<sub>2</sub> in KHCO<sub>3</sub> solutions, *J. Appl. Electrochem.* 36 (2006) 161–172.
- [37] L. Mandal, K.R. Yang, M.R. Motapothu, D. Ren, P. Lobaccaro, A. Patra, M. Sherburne, V.S. Batista, B.S. Yeo, J.W. Ager, J. Martin, T. Venkatesan, Investigating the Role of Copper Oxide in Electrochemical CO<sub>2</sub> Reduction in Real Time, *ACS Appl. Mater. Interfaces* 10 (2018) 8574–8584.
- [38] A. van de Walle, M. Asta, G. Ceder, The alloy theoretic automated toolkit: A user guide, *Calphad* 26 (2002) 539–553.
- [39] P. Giannozzi, S. Baroni, N. Bonini, M. Calandra, R. Car, C. Cavazzoni, D. Ceresoli, G.L. Chiarotti, M. Cococcioni, I. Dabo, A. Dal Corso, S. Fabris, G. Fratesi, S. de Gironcoli, R. Gebauer, U. Gerstmann, C. Gougousis, A. Kokalj, M. Lazzeri, L. Martin-Samos, N. Marzari, F. Mauri, R. Mazzarello, S. Paolini, A. Pasquarello, L. Paulatto, C. Sbraccia, S. Scandolo, G. Sclauzero, A.P. Seitsonen, A. Smogunov, P. Umari, R.M. Wentzcovitch, QUANTUM ESPRESSO: a modular and open-source software project for quantum simulations of materials, *J. Phys.: Condens. Matter* 21 (2009), 395502.
- [40] P. Giannozzi, O. Andreussi, T. Brumme, O. Bunau, M. Buongiorno Nardelli, M. Calandra, R. Car, C. Cavazzoni, D. Ceresoli, M. Cococcioni, N. Colonna, I. Carmineo, A. Dal Corso, S. de Gironcoli, P. Delugas, R.A. DiStasio Jr., A. Ferretti, A. Floris, G. Fratesi, G. Fugallo, R. Gebauer, U. Gerstmann, F. Giustino, T. Gorni, J. Jia, M. Kawamura, H.-Y. Ko, A. Kokalj, E. Küçükbenli, M. Lazzeri, M. Marsili, N. Marzari, F. Mauri, N.L. Nguyen, H.-V. Nguyen, A.P. Seitsonen, A. Smogunov, S. Ponce, D. Rocca, R. Sabatini, B. Santra, M. Schlipf, A.P. Seitsonen, A. Smogunov, I. Timrov, T. Thonhauser, P. Umari, N. Vast, X. Wu, S. Baroni, Advanced capabilities for materials modelling with Quantum ESPRESSO, *J. Phys.: Condens. Matter* 29 (2017), 465901.
- [41] A. van de Walle, G. Ceder, Automating first-principles phase diagram calculations, *JPE* 23 (2002) 348–359.
- [42] F. Raffone, C. Ataca, J.C. Grossman, G. Cicero, MoS<sub>2</sub> Enhanced T-Phase Stabilization and Tunability Through Alloying, *J. Phys. Chem. Lett.* 7 (2016) 2304–2309.
- [43] A.K. Verma, F. Raffone, G. Cicero, Prediction of the structural and electronic properties of Mo<sub>2</sub>Ti<sub>1-x</sub>S<sub>2</sub> monolayers via first principle simulations, *Nanomater. Nanotechnol.* 10 (2020) 1–6.
- [44] J.K. Nørskov, J. Rossmeisl, A. Logadottir, L. Lindqvist, J.R. Kitchin, T. Bligaard, H. Jónsson, Origin of the Overpotential for Oxygen Reduction at a Fuel-Cell Cathode, *J. Phys. Chem. B* 108 (2004) 17886–17892.
- [45] X. Nie, M.R. Esopi, M.J. Janik, A. Asthagiri, Selectivity of CO<sub>2</sub> reduction on copper electrodes: the role of the kinetics of elementary steps, *Angew. Chem. Int. Ed.* 52 (2013) 2459–2462.
- [46] X. Liu, J. Xiao, H. Peng, X. Hong, K. Chan, J.K. Nørskov, Understanding trends in electrochemical carbon dioxide reduction rates, *Nat. Commun.* 8 (2017) 15438.
- [47] B. Zijlstra, X. Zhang, J.-X. Liu, I.A.W. Filot, Z. Zhou, S. Sun, E.J.M. Hensen, First-principles microkinetics simulations of electrochemical reduction of CO<sub>2</sub> over Cu catalysts, *Electrochim. Acta* 335 (2020), 135665.
- [48] X. Liu, P. Schlexer, J. Xiao, Y. Ji, L. Wang, R.B. Sandberg, M. Tang, K.S. Brown, H. Peng, S. Ringe, C. Hahn, T.F. Jaramillo, J.K. Nørskov, K. Chan, pH effects on the electrochemical reduction of CO<sub>2</sub> towards C<sub>2</sub> products on stepped copper, *Nat. Commun.* 10 (2019) 32.
- [49] M. Nolan, S.D. Elliott, Tuning the Transparency of Cu<sub>2</sub>O with Substitutional Cation Doping, *Chem. Mater.* 20 (2008) 5522–5531.
- [50] Y. Jing, Y. Liu, J. Zhao, Z. Xia, Sb<sup>3+</sup> Doping-Induced Triplet Self-Trapped Excitons Emission in Lead-Free Cs<sub>2</sub>SnCl<sub>6</sub> Nanocrystals, *J. Phys. Chem. Lett.* 10 (2019) 7439–7444.
- [51] T. Abendroth, B. Schumm, S.A. Alajlan, A.M. Almogbel, G. Mäder, P. Härtel, H. Althues, S. Kaskel, Optical and thermal properties of transparent infrared blocking antimony doped tin oxide thin films, *Thin Solid Films* 624 (2017) 152–159.

- [52] C.D. Wagner, A.V. Naumkin, A. Kraut-Vass, J.W. Allison, C.J. Powell, J.R. Jr. Rumble, NIST Standard Reference Database 20, Version 3.4 (web version), 2003. (<http://srdata.nist.gov/xps/>).
- [53] M. Biesinger, Advanced analysis of copper X-ray photoelectron spectra: Advanced analysis of copper X-ray photoelectron spectra, *Surf. Interface Anal.* 49 (2017) 1325–1334.
- [54] J.B. Jonathan, E.H. Christopher, A.C. Christopher, R.B. Andrew, Ultrasmall Copper Nanoparticles from a Hydrophobically Immobilized Surfactant Template, *Nano Lett.* 9 (2009) 2239–2242.
- [55] J. Zeng, T. Rino, K. Bejtka, M. Castellino, A. Sacco, M.A. Farkhondeh, A. Chiodoni, F. Drago, C.F. Pirri, Coupled Copper-Zinc Catalysts for Electrochemical Reduction of Carbon Dioxide, *ChemSusChem* 13 (2020) 4128–4139.
- [56] A. Dutta, M. Rahaman, N.C. Luedi, M. Mohos, P. Broekmann, Morphology Matters: Tuning the Product Distribution of CO<sub>2</sub> Electroreduction on Oxide-Derived Cu Foam Catalysts, *ACS Catal.* 6 (2016) 3804–3814.
- [57] C.-T. Dinh, F.P.G. De Arquer, D. Sinton, E.H. Sargent, High Rate, Selective, and Stable Electroreduction of CO<sub>2</sub> to CO in Basic and Neutral Media, *ACS Energy Lett.* 3 (2018) 2835–2840.
- [58] W. Luo, J. Zhang, M. Li, A. Züttel, Boosting CO Production in Electrocatalytic CO<sub>2</sub> Reduction on Highly Porous Zn Catalysts, *ACS Catal.* 9 (2019) 3783–3791.
- [59] M. Ma, K. Liu, J. Shen, R. Kas, W.A. Smith, In Situ Fabrication and Reactivation of Highly Selective and Stable Ag Catalysts for Electrochemical CO<sub>2</sub> Conversion, *ACS Energy Lett.* 3 (2018) 1301–1306.
- [60] Y. Chen, C.W. Li, M.W. Kanan, Aqueous CO<sub>2</sub> reduction at very low overpotential on oxide-derived Au nanoparticles, *J. Am. Chem. Soc.* 134 (2012) 19969–19972.
- [61] J. Rosen, G.S. Hutchings, Q. Lu, S. Rivera, Y. Zhou, D.G. Vlachos, F. Jiao, Mechanistic Insights into the Electrochemical Reduction of CO<sub>2</sub> to CO on Nanostructured Ag Surfaces, *ACS Catal.* 5 (2015) 4293–4299.
- [62] Q. Lu, J. Rosen, Y. Zhou, G.S. Hutchings, Y.C. Kimmel, J.G. Chen, F. Jiao, A selective and efficient electrocatalyst for carbon dioxide reduction, *Nat. Comm.* 5 (2014) 3242.
- [63] M. Dunwell, Q. Lu, J.M. Heyes, J. Rosen, J.G. Chen, Y. Yan, Feng Jiao, B. Xu, The Central Role of Bicarbonate in the Electrochemical Reduction of Carbon Dioxide on Gold, *J. Am. Chem. Soc.* 139 (2017) 3774–3783.
- [64] A.J. Garza, A.T. Bell, M. Head-Gordon, Is Subsurface Oxygen Necessary for the Electrochemical Reduction of CO<sub>2</sub> on Copper? *J. Phys. Chem. Lett.* 9 (2018) 601–606.
- [65] S.B. Scott, T.V. Hogg, A.T. Landers, T. Maagaard, E. Bertheussen, J.C. Lin, R. C. Davis, J.W. Beeman, D. Higgins, W.S. Drisdell, C. Hahn, A. Mehta, B. Seger, T. F. Jaramillo, I. Chorkendorff, Absence of Oxidized Phases in Cu under CO Reduction Conditions, *ACS Energy Lett.* 4 (2019) 803–804.
- [66] Y. Lum, J.W. Ager, Stability of Residual Oxides in Oxide-Derived Copper Catalysts for Electrochemical CO<sub>2</sub> Reduction Investigated with <sup>18</sup>O Labeling, *Angew. Chem. Int. Ed.* 57 (2018) 551–554.
- [67] Q. Lei, H. Zhu, K. Song, N. Wei, L. Liu, D. Zhang, J. Yin, X. Dong, K. Yao, N. Wang, X. Li, B. Davaasuren, J. Wang, Y. Han, Investigating the Origin of Enhanced C<sub>2+</sub> Selectivity in Oxide-/Hydroxide-Derived Copper Electrodes during CO<sub>2</sub> Electroreduction, *J. Am. Chem. Soc.* 142 (2020) 4213–4222.
- [68] S. Jiang, K. Klingan, C. Pasquini, H. Dau, New aspects of operando Raman spectroscopy applied to electrochemical CO<sub>2</sub> reduction on Cu foams, *J. Chem. Phys.* 150 (2019), 041718.
- [69] M. Dunwell, W. Luc, Y. Yan, F. Jiao, B. Xu, Understanding Surface-Mediated Electrochemical Reactions: CO<sub>2</sub> Reduction and Beyond, *ACS Catal.* 8 (2018) 8121–8129.
- [70] J.A. Gauthier, M. Fields, M. Bajdich, L.D. Chen, R.B. Sandberg, K. Chan, J. K. Nørskov, Facile Electron Transfer to CO<sub>2</sub> during Adsorption at the Metal|Solution Interface, *J. Phys. Chem. C* 123 (2019) 29278–29283.
- [71] P.S. Lamoureux, A.R. Singh, K. Chan, pH Effects on Hydrogen Evolution and Oxidation over Pt(111): Insights from First-Principles, *ACS Catal.* 9 (2019) 6194–6201.
- [72] V. Grozovski, S. Veszteg, G. Láng, P. Broekmann, Electrochemical Hydrogen Evolution: H<sup>+</sup> or H<sub>2</sub>O Reduction? A Rotating Disk Electrode Study, *J. Electrochem. Soc.* 164 (2017) E3171–E3178.